Publication Year	2018
Acceptance in OA@INAF	
Title	First Measurement of the 14N/15N Ratio in the Analog of the Sun Progenitor OMC-2 FIR4
Authors	Kahane, Claudine; Jaber Al-Edhari, Ali; Ceccarelli, Cecilia; López-Sepulcre, Ana; FONTANI, FRANCESCO; et al.
DOI	10.3847/1538-4357/aa9e88
Handle	http://hdl.handle.net/20.500.12386/27820
Journal	THE ASTROPHYSICAL JOURNAL
Number	852

Draft version December 6, 2017
Typeset using LaTeX default style in AASTeX61

FIRST MEASUREMENT OF THE $^{14}N/^{15}N$ RATIO IN THE ANALOGUE OF THE SUN PROGENITOR OMC-2 FIR4

Claudine Kahane,[1] Ali Jaber Al-Edhari,[1, 2] Cecilia Ceccarelli,[1] Ana López-Sepulcre,[3] Francesco Fontani,[4]
and Mihkel Kama[5]

[1] *Univ. Grenoble Alpes, CNRS, IPAG, 122 rue de la Piscine, 38000 Grenoble, France*
[2] *University of Al-Muthanna, College of Science, Physics Department, Al-Muthanna, Iraq*
[3] *Institut de Radioastronomie Millimetrique, 300 rue de la Piscine, 38406, Saint-Martin d'Heres, France*
[4] *INAF-Osservatorio Astrofisico di Arcetri, Largo E. Fermi 5, I-50125, Florence, Italy*
[5] *Institute of Astronomy, University of Cambridge, Madingley Road, Cambridge CB3 0HA, UK*

(Received 2017; Revised; Accepted December 6, 2017)

Submitted to ApJ

ABSTRACT

We present a complete census of the $^{14}N/^{15}N$ isotopic ratio in the most abundant N-bearing molecules towards the cold envelope of the protocluster OMC-2 FIR4, the best known Sun progenitor. To this scope, we analysed the unbiased spectral survey obtained with the IRAM-30m telescope at 3mm, 2mm and 1mm. We detected several lines of CN, HCN, HNC, HC_3N, N_2H^+, and their respective ^{13}C and ^{15}N isotopologues. The lines relative fluxes are compatible with LTE conditions and moderate line opacities have been corrected via a Population Diagram method or theoretical relative intensity ratios of the hyperfine structures. The five species lead to very similar $^{14}N/^{15}N$ isotopic ratios, without any systematic difference between amine and nitrile bearing species as previously found in other protostellar sources. The weighted average of the $^{14}N/^{15}N$ isotopic ratio is 270 ± 30. This $^{14}N/^{15}N$ value is remarkably consistent with the [250−350] range measured for the local galactic ratio but significantly differs from the ratio measured in comets (around 140). High-angular resolution observations are needed to examine whether this discrepancy is maintained at smaller scales. In addition, using the CN, HCN and HC_3N lines, we derived a $^{12}C/^{13}C$ isotopic ratio of 50 ± 5.

Keywords: astrochemistry – stars: formation – stars: low-mass – stars: protostars (OMC-2) – ISM: abundances

Corresponding author: Claudine Kahane
claudine.kahane@univ-grenoble-alpes.fr

1. INTRODUCTION

The Solar System is the result of a long and complex process, several aspects of which still remain a mistery. One of these is the so-called "anomalous" ^{14}N/^{15}N value in the objects of the Solar System (Caselli & Ceccarelli 2012; Hily-Blant et al. 2013). Based on the solar wind particles (Marty 2012), the Solar Nebula value is 441 ± 6. However, ^{14}N/^{15}N is 272 in the Earth atmosphere (Marty 2012), around 140 in comets (Manfroid et al. 2009; Mumma & Charnley 2011; Shinnaka et al. 2014; Rousselot et al. 2014), and between 5 and 300 in meteorites (Busemann et al. 2006; Bonal et al. 2010; Aléon 2010). The Solar System primitive objects as well as the terrestrial atmosphere are, hence, enriched of ^{15}N with respect to the presumed initial value. It has been long known that, similarly to the ^{15}N enrichment, the D/H ratio in terrestrial water is about ten times larger than in the Solar Nebula and this is very likely due to the conditions in the earliest phases of the Solar System (see e.g. the reviews by Ceccarelli et al. (2014a) and Cleeves et al. (2015)). The reason for the ^{15}N enrichment has, thus, been searched for in the chemical evolution of matter during the first steps of the Solar System formation (e.g. Terzieva & Herbst (2000); Rodgers & Charnley (2008); Wirström et al. (2012); Hily-Blant et al. (2013)).

Several observations in Solar-like star forming regions have been reported in the literature. In prestellar cores, ^{14}N/^{15}N varies between 70 and more than 1000 (Ikeda et al. (2002); Gerin et al. (2009); Milam & Charnley (2012); Daniel et al. (2013); Hily-Blant et al. (2013, 2017); Bizzocchi et al. (2013); Taniguchi & Saito (2017)), in Solar-like Class 0 protostars between 150 and 600 (Gerin et al. 2009; Wampfler et al. 2014), and 80−160 in protoplanetary disks (Guzmán et al. 2015, 2017).

Whereas the ^{14}N/^{15}N values reported in the literature for prestellar cores, protostars, disks and comets have been derived from the observations of half a dozen of different species (CN, HCN, HNC, NH_3, N_2H^+, cyanopolyynes), it should be noted that, for each of these objects, only a few species were used each time.

Nonetheless, one has to consider that, rather than to the Solar Nebula ^{14}N/^{15}N value, these measurements should be compared to the nowadays local interstellar ^{14}N/^{15}N ratio of ~ 300, which results from cosmic evolution in the solar neighbourhood (Romano et al. (2017); Hily-Blant et al. (2017) and references therein) and is, apparently by coincidence, very close to the terrestrial atmosphere value.

In order to understand the origin of the Solar System ^{15}N enrichment, we need to measure it in objects that are as most as possible similar to the Sun progenitor. The so far known best analogue of the Sun progenitor is represented by the source OMC-2 FIR4, in the Orion Molecular Complex at a distance of 420 pc (Menten et al. 2007; Hirota et al. 2007), north of the famous KL object. Several recent observations show that FIR4 is a young protocluster containing several protostars, some of which will eventually become Suns (Shimajiri et al. 2008; López-Sepulcre et al. 2013; Furlan et al. 2014). In addition, OMC-2 FIR4 shows signs of the presence of one or more sources of energetic ≥ 10 MeV particles, the dose of which is similar to that measured in meteoritic material (Ceccarelli et al. 2014b; Fontani et al. 2017). In this article, we report the first measure of the ^{14}N/^{15}N ratio in OMC-2 FIR4, using different molecules: HC_3N, HCN, HNC, CN and N_2H^+.

2. OBSERVATIONS

We carried out an unbiased spectral survey of OMC-2 FIR4 (PI: Ana López-Sepulcre) in the 1,2 and 3mm bands with the IRAM 30 m telescope. The 3 mm (80.5−116.0 GHz) and 2 mm (129.2−158.8 GHz) bands were observed between 31 Aug. and 5 Sep. 2011, and on 24 Jun. 2013. The 1 mm (202.5−266.0 GHz) range was observed on 10−12 Mar. 2012 and on 7 Feb. 2014. The Eight MIxer Receiver (EMIR) has been used, connected to the 195 kHz resolution Fourier Transform Spectrometer (FTS) units. The observations were conducted in wobbler switch mode, with a throw of 120″. Pointing and focus measurements were performed regularly. The telescope Half Power Beam Width (HPBW) is 21−30.6″, 15.5−19″ and 9−12″ in the 1,2 and 3mm bands respectively. The package CLASS90 of the GILDAS software collection[1] was used to reduce the data. The uncertainties of calibration are estimated to be lower than 10% at 3 mm and 20% at 2 mm and 1mm. After subtraction of the continuum emission via first-order polynomial fitting, a final spectrum was obtained by stitching the spectra from each scan and frequency setting. The intensity was converted from antenna temperature ($T^*_{\rm ant}$) to main beam temperature ($T_{\rm mb}$) using the beam efficiencies provided at the IRAM web site. The typical rms noise, expressed in $T_{\rm mb}$ unit, is 4−7 mK in the 3mm band, 8−10mK in the 2mm band, and 15−25mK in the 1mm band.

---

[1] http://www.iram.fr/IRAMFR/GILDAS/

3. RESULTS

In order to derive the ^{14}N/^{15}N ratio in OMC-2 FIR4, we have looked for the ^{15}N-bearing substitutes of all the abundant N-bearing species present in the survey. We have clearly detected and identified the ^{15}N-isotopologues of five species: HC_3N, HCN, HNC, CN, N_2H^+, most with more than one line, and tentatively detected one line of $H^{13}C^{15}N$. In addition, we have also included in our analysis the ^{13}C-bearing isotopes of HC_3N, HCN, HNC and CN. A representative sample of these lines is shown in Fig. 1 and all the observed lines are plotted in the Appendix in Figs. 4 to 12.

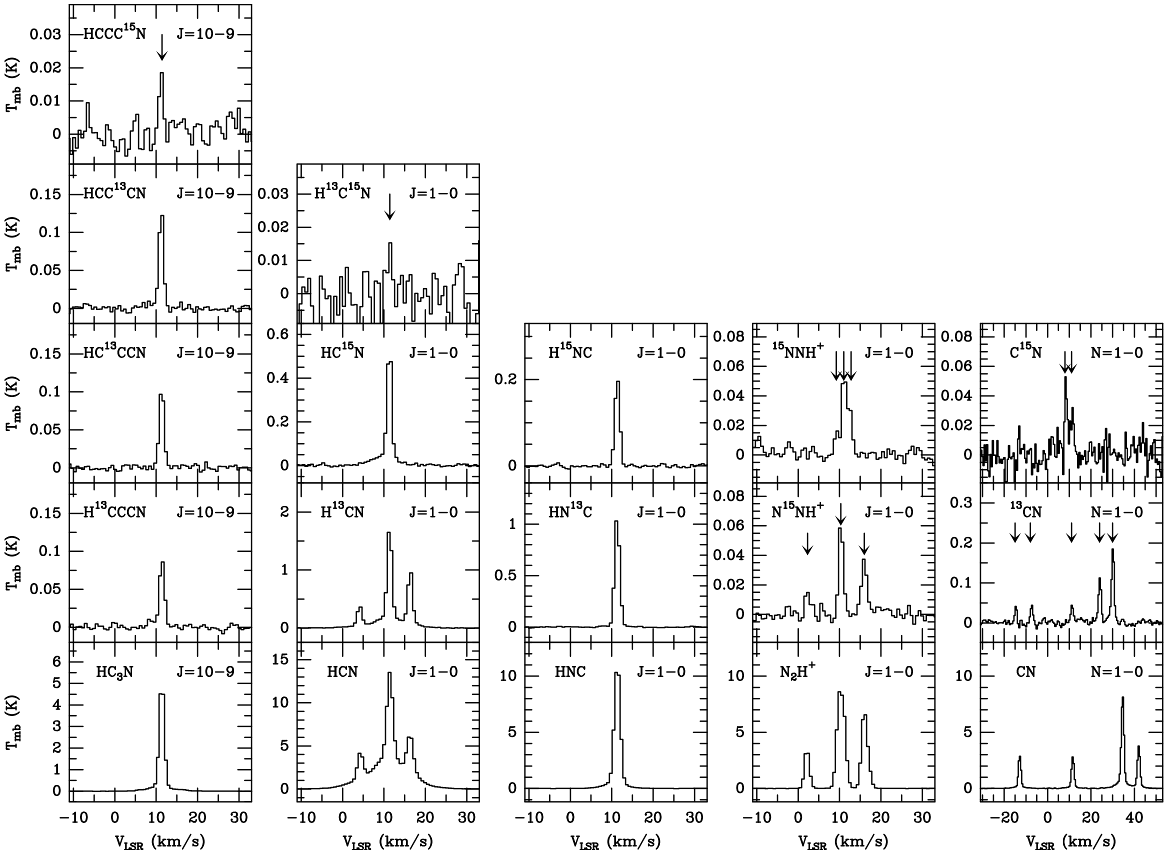

Figure 1. Representative sample of the observed spectra for the HC_3N, HCN, HNC, N_2H^+ and CN families. The temperature scale is main beam temperature. Weak lines are indicated by an arrow.

The lines analysis and modeling presented here make use of several tools of the CASSIS package.[2] Gaussian fits have been used to derive the lines integrated intensities (called fluxes in the following) and kinematical properties. All lines are well fitted with narrow Gaussian components showing low dispersions in central velocities and linewidths (V_{LSR} = 11.3 (0.1) km.s^{-1}, FWHM = 1.4 (0.2) km.s^{-1}). In addition, the strongest lines also show a slightly displaced broad component (V_{LSR} = 10.8 (0.3) km.s^{-1}, FWHM = 6.4 (0.4) km.s^{-1} from Gaussian fits), which is not detected in the ^{15}N-bearing species, except in HC^{15}N. We have, thus, focussed our work on the narrow component. Figs. 4 to 12 of the Appendix show the Gaussian profiles superimposed to the observed lines. The fluxes reported in Table 1 to Table 4 correspond to the narrow Gaussian components only and the 1 sigma error bars include the fit and the calibration uncertainties.

For HCN, HNC and N_2H^+, our survey covers only the $(J = 1 - 0)$ transitions of the ^{15}N-bearing isotopologues. Thus, for these species, to derive of the ^{14}N/^{15}N ratio we used the "flux ratio method" applied to the $(J = 1 - 0)$ transitions of the observed isotopologues. It leads to reliable abundance ratios provided that (i) the $(1 - 0)$ transitions

---

[2] (CASSIS:Centre d'Analyse Scientifique de Spectres Instrumentaux et Synthtiques): is a line analysis and modeling software developed by IRAPUPS/CNRS (*http://cassis.irap.omp.eu*)

of the various isotopologues correspond to the same excitation temperature, (ii) the lines are not significantly affected by or can be corrected for opacity effects, (iii) the emission size is the same for the various isotopologues.

For HC_3N and CN, since more than one rotational transition is observed for the ^{15}N-bearing isotopologues, we could perform a Local Thermal Equilibrium (LTE) modeling to derive the $^{14}N/^{15}N$ abundance ratios, as discussed for each species below.

Whenever possible, we have obtained direct $^{14}N/^{15}N$ measurements. In two cases, HCN and HNC, we have obtained indirect $^{14}N/^{15}N$ derivations from the less abundant isotopologues $H^{13}CN$ and $HN^{13}C$, assuming a $^{12}C/^{13}C$ ratio.

In all cases, the isotopic ratios that we derive are beam-averaged values, at the scale of the largest HPBW of our observations (∼ 30").

3.1. *HC_3N*

To rely on a coherent set of lines, likely to sample the same gas, we have restricted our analysis to the narrow HC_3N emission, because broad emission from the ^{15}N and the ^{13}C isotopes of HC_3N is not detected in our survey.

Table 1. Integrated intensities from Gaussian fits for HC_3N and its isotopologues.

HC_3N				$H^{13}CCCN$	$HC^{13}CCN$	$HCC^{13}CN$	$HCCC^{15}N$
Transition ($J' - J$)	Frequency$^{(1)}$ [MHz]	$E_{up}^{(1)}$ [K]	$\int T_{mb}dv$ [K.km.s^{-1}]	$\int T_{mb}dv$ [K.km.s^{-1}]	$\int T_{mb}dv$ [K.km.s^{-1}]	$\int T_{mb}dv$ [K.km.s^{-1}]	$\int T_{mb}dv$ [K.km.s^{-1}]
9−8	81881.5	19.6	7.1(0.7)	-	0.11(0.01)	0.16(0.02)	-
10−9	90979.0	24.0	7.4(0.7)	0.14(0.01)	0.16(0.02)	0.18(0.02)	0.024(0.007)
11−10	100076.4	28.8	7.3(0.7)	0.15(0.02)	0.16(0.02)	0.19(0.02)	0.028(0.006)
12−11	109173.6	34.0	7.4(0.7)	0.14(0.01)	0.17(0.02)	0.18(0.02)	0.030(0.010)
13−12	114615.0$^{(2)}$	38.5$^{(2)}$	-	0.11(0.01)	-	-	-
15−14	136464.4	52.4	5.7(1.1)	-	0.10(0.02)	0.13(0.03)	-
16−15	145561.0	59.4	4.7(0.9)	0.08(0.02)	0.10(0.02)	0.12(0.02)	-
17−16	154657.3	66.8	3.7(0.7)	0.08(0.02)	0.06(0.01)	0.13(0.03)	-
24−23	218324.7	130.9	0.6(0.1)	-	-	-	-
26−25	236512.8	153.2	0.36(0.07)	-	-	-	-
27−26	245606.3	165.0	0.37(0.07)	-	-	-	-
29−28	263792.3	189.9	0.22(0.04)	-	-	-	-

The integrated intensities correspond to the narrow Gaussian components only and the 1 σ error bars include the fit and the calibration uncertainties.

(1) We report in this table only the main isotopologue frequencies and upper level energies, except for the (13−12) transition, which falls outside the observed frequency range.

(2) These values correspond to the $H^{13}CCCN$ isotopologue, the only one for which the (13−12) transition is covered by our observations.

To derive the column densities of the five species, we have performed a Population Diagram analysis of the lines reported in Table 1, which corrects iteratively for the opacity effects. Large scale maps obtained recently with the IRAM 30m telescope (Jaber Al-Edhari et al., in prep.) show that the cyanopolyyne emission is extended. Thus, no beam dilution correction has been applied. The results of the analysis are shown in Fig. 2.

The HC_3N lines diagram suggests the existence of two components responsible for the narrow emission. After correction of their (moderate) opacity (0.20 to 0.25), the HC_3N lines with upper level energy E_{up} lower than 130 K are compatible with an LTE excitation at a rotational temperature of 25 K, in agreement with the values derived from the ^{13}C isotopes, and a HC_3N column density of 3.3×10^{13} cm^{-2}. Assuming the same excitation temperature for the $HCCC^{15}N$ lines, we obtain a column density of 1.2×10^{11} cm^{-2} and a direct determination of the $^{14}N/^{15}N$ abundance ratio of 275 ± 65. For the three ^{13}C-bearing isotopologues of HC_3N, we derive, in the same way, $^{12}C/^{13}C$ abundance ratios of 57 ± 7, 59 ± 11 and 46 ± 6. We have checked that an LTE model based on these parameters is perfectly coherent with the non detection of the isotopologues lines at $E_{up} > 70$ K.

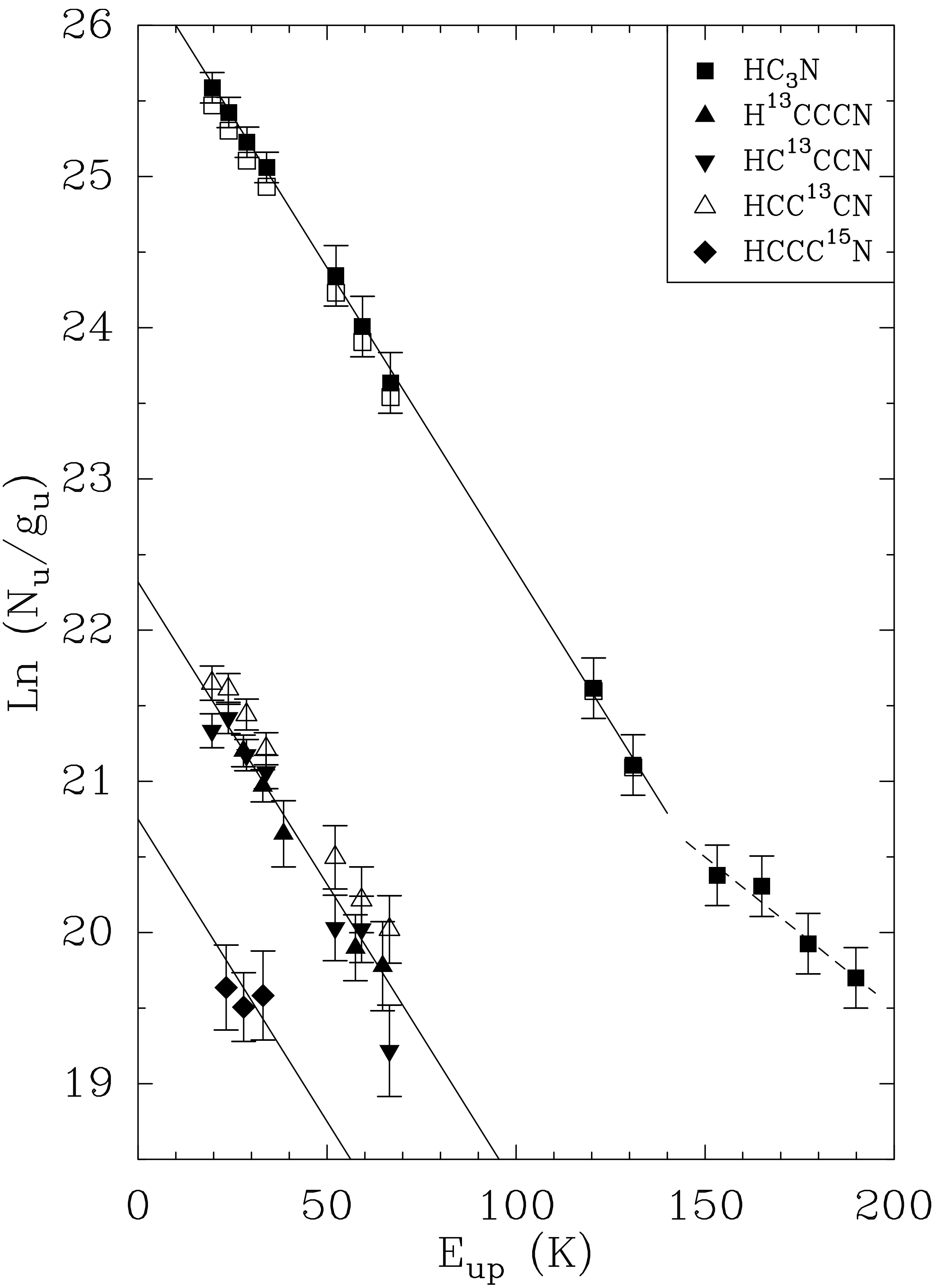

Figure 2. Population Diagrams for HC$_3$N and its isotopologues. No beam dilution correction has been applied. The HC$_3$N data points are shown as black squares when corrected for opacity effects and as empty squares without the opacity correction. The three solid lines correspond to a rotational temperature of 25 K; the dashed line corresponds to an excitation temperature of 50 K.

The HC_3N lines with E_{up} >150 K suggest the existence of a warmer component but its analysis is out of the scope of this article. An extended and detailed modeling of the cyanopolyynes emission in OMC-2 FIR4, relying on a more complete set of data and including the broad emission, is presented in another study (Jaber Al-Edhari et al., in prep.).

3.2. *HCN*

The lines of HCN and of its ^{13}C- and ^{15}N- bearing isotopologues show a narrow and a broad emission. We have fitted them by Gaussian profiles (see Table 2 and Fig. 9).

Table 2. Integrated intensities from Gaussian fits for HCN and its isotopologues.

HCN					$H^{13}CN$	$HC^{15}N$	$H^{13}C^{15}N$
Transition ($J'_{F'} - J_F$) or ($J' - J$) $^{(1)}$	Frequency$^{(2)}$ [MHz]	$E_{up}^{(2)}$ [K]	Component$^{(3)}$	$\int T_{mb}dv^{(4)}$ [K.km.s^{-1}]	$\int T_{mb}dv^{(4)}$ [K.km.s^{-1}]	$\int T_{mb}dv^{(4)}$ [K.km.s^{-1}]	$\int T_{mb}dv^{(4)}$ [K.km.s^{-1}]
$1_1 - 0_1$	88630.4	4.3	N	8.4(0.9)	1.3(0.1)	-	-
$1_2 - 0_1$ or $1 - 0$	88631.9	4.3	N	13(2)	2.2(0.2)	0.70(0.07)	0.020(0.008)
			B	50 (5)	2.0 (0.2)	0.34 (0.03)	-
$1_0 - 0_1$	88633.9	4.3	N	5.2(0.5)	0.44(0.06)	-	-
$3 - 2$	265886.4	25.2	N	24(1)	1.3(0.3)	-	-
			B	85(18)	7.2(1.5)	-	-

(1) For the ^{15}N-bearing isotopologues and the broad Gaussian component, the reported transition is the ($J = 1 - 0$) one.

(2) We report in this table only the main isotopologue frequencies and upper level energies.

(3) Narrow (N) and broad (B) Gaussian components fitted to the observed spectra, with no attempt to distinguish the hyperfine components in the broad emission.

(4) The 1 σ error bars include the fit and the calibration uncertainties.

3.2.1. *Narrow emission*

The ($J = 1 - 0$) spectra of HCN and $H^{13}CN$ split into three hyperfine components, which provides a measure of the line opacity when comparing the relative intensities of the hyperfine components. Under LTE optically thin conditions, this ratio is 1:3:5. Relative to the weakest component, the observed flux ratios obtained for HCN and $H^{13}CN$ are respectively 1:(1.6±0.2):(2.6±0.5) and 1:(2.9±0.5):(5.1±0.9) (see Table 5). It suggests that the $H^{13}CN$ hyperfine components have the same excitation temperature and are optically thin, whereas the HCN lines suffer from significant opacity or/and anomalous excitation effects, which will prevent from a direct determination of the $^{14}N/^{15}N$ ratio. Neglecting the weak differences of line frequencies, the double isotopic ratio $^{13}C^{14}N/^{12}C^{15}N$ is then simply equal to the ratio of the total fluxes, obtained by adding the hyperfine component contributions: 5.6 ± 0.8. This may lead to an indirect determination of the $^{14}N/^{15}N$ ratio, assuming a $^{12}C/^{13}C$ ratio. In addition, the $H^{13}C^{15}N$ $(1-0)$ line being tentatively detected (at 2.5 sigmas, see Fig. 1 and Fig. 9), the comparison with the $H^{13}C^{14}N$ $(1-0)$ total flux provides a direct measurement of the $^{14}N/^{15}N$ ratio, equal to 200 ± 85, whereas the comparison with the $HC^{15}N$ $(1-0)$ flux gives a $^{12}C/^{13}C$ ratio of 36 ± 15. It should be noted that these ratios may be somewhat underestimated, the $H^{13}C^{15}N$ $(1-0)$ line being only tentatively detected, which tends to an overestimation of its flux.

In addition, the Population Diagram built with the $J = (1-0)$ and $(2-1)$ fluxes of $H^{13}CN$ leads to an excitation temperature of 6 K, if the emission is assumed to be more extended than the largest beam ($30''$), a reasonable assumption for such cold gas.

3.2.2. *Broad emission*

The broad emission is particularly evident in the ($J = 2 - 1$) spectra of HCN and $H^{13}CN$, but it is also detected in the ($J = 1 - 0$) emission, even for $HC^{15}N$. We have estimated the corresponding $^{13}C^{14}N/^{12}C^{15}N$ double isotopic ratio from the ($J = 1 - 0$) line flux ratio. This value, 6.0 ± 1.5, shows a quite large uncertainty but is fully compatible with the ratio derived from the narrow emission. A Population Diagram applied to the $H^{13}CN$ ($J = 1 - 0$) and ($J = 2 - 1$) fluxes, with no beam dilution, leads to an excitation temperature of 22 K, which suggests that this broad emission could come from a warmer component than the narrow one.

3.3. *HNC*

The broad emission, which is marginally visible in the HNC $(1-0)$ and HN^{13}C $(2-1)$ spectra only, has not been included in our analysis (see Table 3 and Fig. 10). The HNC hyperfine structure is too narrow to be spectrally resolved in our data. However, a Population Diagram analysis applied to the $(J = 1-0)$ and $(2-1)$ lines of HN^{13}C, assuming extended emission, indicates moderate opacities (∼0.2) and leads to an excitation temperature of 7−8 K. Such a low excitation temperature appears coherent with the assumption of extended emission.

As the HNC line is certainly more severely affected by opacity effect, a direct derivation of the ^{14}N/^{15}N ratio is not possible. From the flux ratio of ^{13}C- and ^{15}N- bearing species, the double isotopic ratio ^{13}C^{14}N/^{12}C^{15}N equal to 5.4 ± 0.8, becomes 6.0 ± 0.8 when the opacity correction is applied to the HN^{13}C line flux.

Table 3. Integrated intensities from Gaussian fits for HNC, N$_2$H$^+$ and their isotopologues.

HNC				HN^{13}CN		H^{15}NC	
Transition $(J'-J)$	E$_{up}$ [K]	Frequency [MHz]	$\int$T$_{mb}$dv [K.km.s^{-1}]	Frequency [MHz]	$\int$T$_{mb}$dv [K.km.s^{-1}]	Frequency [MHz]	$\int$T$_{mb}$dv [K.km.s^{-1}]
$1-0$	4.4	90663.6	21(2)	87090.9	1.7(0.2)	88865.7	0.31(0.01)
$3-2$	25.1		-	261263.3	1.09(0.04)		-
N$_2$H$^+$				^{15}NNH$^+$		N^{15}NH$^+$	
Transition $(J'_{F'}-J_F)$	E$_{up}$ [K]	Frequency [MHz]	$\int$T$_{mb}$dv [K.km.s^{-1}]	Frequency$^{(1)}$ [MHz]	$\int$T$_{mb}$dv [K.km.s^{-1}]	Frequency$^{(1)}$ [MHz]	$\int$T$_{mb}$dv [K.km.s^{-1}]
1_1-0_1	4.5	93171.9	13.1(1.5)	90263.5	0.08(0.01)	91204.3	0.059(0.008)
1_2-0_1	4.5	93173.7	21.3(2.5)	90263.9	0.036(0.005)	91206.0	0.09(0.02)
1_0-0_1	4.5	93176.1	5.3(0.5)	90264.5	0.015(0.004)	91208.5	0.025(0.006)

The integrated intensities correspond to the narrow Gaussian components only and the 1 σ error bars include the fit and the calibration uncertainties.

(1) Frequencies from Dore et al. (2009).

3.4. *N$_2$H$^+$*

The main isotope and each of the ^{15}N-bearing substitutes of N$_2$H$^+$ show three hyperfine components, with relative intensities of 1:3:5 if LTE optically thin emission applies (see Table 5). The frequencies of the hyperfine lines of ^{15}NNH$^+$ and N^{15}NH$^+$ have been presented by Dore et al. (2009). The observed hyperfine flux ratios are 1:(2.5±0.4):(4.1±0.6) for the main isotopologue, 1:(2.4±0.7):(5.0±1.5) for ^{15}NNH$^+$ and 1:(2.4±0.6):(3.8±1.2) for N^{15}NH$^+$. We conclude that, as expected, the emission of the ^{15}N-bearing species is optically thin and that the lines opacity is very moderate for the main isotopologue components. Assuming that the weakest line of N$_2$H$^+$ $(1-0)$ is optically thin, we can estimate the opacity corrected fluxes of the two others. With such a correction, the ^{14}N/^{15}N ratios derived from the total fluxes are 320 ± 60 from ^{15}NNH$^+$ and 240 ± 50 from N^{15}NH$^+$.

3.5. *CN*

The CN family members present extremely rich rotational spectra, combining fine and hyperfine structure interactions and our survey covers both the $(N = 1-0)$ and $(N = 2-1)$ transitions for the three isotopologues (see Figs. 11 and 12).

In addition, the main isotopologue shows a broad emission, more visible on the $(N = 2-1)$ transitions than on the $(N = 1-0)$ ones.

Most of the CN $(N = 1-0)$ and $(N = 2-1)$ hyperfine components reported in the CDMS and JPL databases are easily detected. We have compared the observed flux ratios with the theoretical ratios (proportional to the g$_{up}$. A$_{ij}$ ratios, the slight frequency differences being neglected). The results (see Table 5) suggest that the hyperfine components follow an intensity distribution very close to LTE and that the line opacities are moderate.

The same analysis shows that the ^{13}CN and C^{15}N $(N = 1-0)$ and $(N = 2-1)$ which are clearly detected and do not suffer from blending follow an intensity distribution very close to LTE and that the lines are optically thin.

We have thus performed a simultaneous LTE modeling of the ($N = 1 - 0$) and ($N = 2 - 1$) transitions for the three isotopologues. For ^{13}CN and C^{15}N we have assumed that the emission comes from a single extended component whose kinematical properties are derived from the gaussian fits (V$_{LSR}$ = 11.4 km.s^{-1}, FWHM = 1.3 km.s^{-1}). For CN, to account for the broad emission, we have added a second component (V$_{LSR}$ = 11.1 km.s^{-1}, FWHM = 6.9 km.s^{-1}). The free parameters of our modelling, performed with a Markov Chain Monte-Carlo (MCMC) minimization to obtain the best fit to the lines, were the excitation temperature T_{ex} and the column densities of the three isotopologues for the narrow emission component, the source size, the CN column density and the excitation temperature for the broad CN emission component.

For the first component, the best fit was obtained with the following parameters: $T_{ex} = 8 \pm 1$ K, N(CN) = (3.5±0.5)×10^{14} cm^{-2}, N(^{13}CN) = (8±1)×10^{12} cm^{-2}, N(C^{15}N) = (1.3±0.2)×10^{12} cm^{-2}. It corresponds to the following isotopic ratios: ^{13}C^{14}N/^{12}C^{15}N $= 6.2 \pm 1.3$, ^{12}C/^{13}C $= 44 \pm 8$ and ^{14}N/^{15}N $= 270 \pm 60$.

For the broad component, there are three free parameters and the best fit solution is degenerate. However, the excitation temperature depends only weakly on the assumed size and is between 50 and 60 K.

The calculated profiles are superimposed to the observed ones in Figs. 11 and Fig. 12.

Table 4. Integrated intensities from Gaussian fits for CN and its isotopologues

Species	Transition$^{(1)}$	Frequency	E$_{up}$	V$_{LSR}$	FWHM	$\int$T$_{mb}$dv
	$N_{J'F'1F'} - N_{JF1F}$ or $N'_{J'F'} - N_{JF}$	[MHz]	[K]	[km.s^{-1}]	[km.s^{-1}]	[K.km.s^{-1}]
CN	$1_{0\ 1/2\ 1/2} - 0_{0\ 1/2\ 1/2}$	113123.37	5.43	11.6(0.3)	1.4(0.3)	0.9(0.1)
	$1_{0\ 1/2\ 1/2} - 0_{0\ 1/2\ 3/2}$	113144.19	5.43	11.7(0.3)	1.5(0.3)	4.9(0.5)
	$1_{0\ 1/2\ 3/2} - 0_{0\ 1/2\ 1/2}$	113170.54	5.43	11.7(0.3)	1.5(0.3)	5.3(0.5)
	$1_{0\ 1/2\ 3/2} - 0_{0\ 1/2\ 3/2}$	113191.33	5.43	11.7(0.3)	1.5(0.3)	5.6(0.6)
	$1_{0\ 3/2\ 3/2} - 0_{0\ 1/2\ 1/2}$	113488.14	5.45	11.7(0.3)	1.5(0.3)	6.0(0.7)
	$1_{0\ 3/2\ 5/2} - 0_{0\ 1/2\ 3/2}$	113490.99	5.45	11.7(0.3)	1.6(0.3)	14.0(1.6)
	$1_{0\ 3/2\ 1/2} - 0_{0\ 1/2\ 1/2}$	113499.64	5.45	11.6(0.3)	1.4(0.3)	4.3(0.4)
	$1_{0\ 1/2\ 1/2} - 0_{0\ 1/2\ 3/2}$	113508.93	5.45	11.7(0.3)	1.4(0.3)	4.5(0.5)
	$1_{0\ 3/2\ 1/2} - 0_{0\ 1/2\ 3/2}$	113520.42	5.45	11.6(0.3)	1.3(0.3)	0.8(0.1)
	$2_{0\ 3/2\ 1/2} - 1_{0\ 3/2\ 1/2}$	226287.43	16.31	11.3(0.1)	1.1(0.1)	0.5(0.1)
	$2_{0\ 3/2\ 1/2} - 1_{0\ 3/2\ 3/2}$	226298.92	16.31	11.0(0.2)	1.6(0.2)	0.6(0.2)
	$2_{0\ 3/2\ 3/2} - 1_{0\ 3/2\ 1/2}$	226303.08	16.31	11.3(0.1)	1.2(0.1)	0.5(0.1)
	$2_{0\ 3/2\ 3/2} - 1_{0\ 3/2\ 3/2}$	226314.54	16.31	11.2(0.1)	1.1(0.1)	1.0(0.2)
	$2_{0\ 3/2\ 3/2} - 1_{0\ 1/2\ 5/2}$	226332.54	16.31	11.3(0.1)	1.1(0.1)	0.5(0.1)
	$2_{0\ 3/2\ 5/2} - 1_{0\ 3/2\ 3/2}$	226341.93	16.31	11.3(0.1)	1.1(0.1)	0.7(0.1)
	$2_{0\ 3/2\ 5/2} - 1_{0\ 3/2\ 5/2}$	226359.87	16.31	11.3(0.1)	1.2(0.1)	2.6(0.6)
	$2_{0\ 3/2\ 1/2} - 1_{0\ 1/2\ 3/2}$	226616.56	16.31	11.3(0.1)	1.1(0.1)	0.5(0.1)
	$2_{0\ 3/2\ 3/2} - 1_{0\ 1/2\ 3/2}$	226632.19	16.31	11.3(0.1)	1.3(0.1)	3.2(0.7)
	$2_{0\ 3/2\ 5/2} - 1_{0\ 1/2\ 3/2}$	226659.58	16.31	11.4(0.1)	1.6(0.1)	8.3(1.7)
	$2_{0\ 3/2\ 1/2} - 1_{0\ 1/2\ 1/2}$	226663.70	16.31	11.4(0.1)	1.4(0.1)	3.2(0.7)
	$2_{0\ 3/2\ 3/2} - 1_{0\ 1/2\ 1/2}$	226679.38	16.31	11.4(0.1)	1.3(0.1)	3.6(0.8)
	$2_{0\ 5/2\ 5/2} - 1_{0\ 3/2\ 5/2}$	226892.12	16.34	11.3(0.1)	1.2(0.1)	3.2(0.7)
	$2_{0\ 5/2\ 3/2} - 1_{0\ 3/2\ 5/2}$	226905.38	16.34	11.3(0.2)	0.9(0.2)	0.10(0.03)
^{13}CN	$1_{1/2\ 0\ 1} - 0_{1/2\ 1\ 1}$	108412.86	5.23	11.0(0.4)	1.1(0.4)	0.03(0.01)

Table 4 continued on next page

Table 4 *(continued)*

Species	Transition$^{(1)}$	Frequency	E_{up}	V_{LSR}	FWHM	$\int T_{mb}dv$
	$N_{J'F'1F'} - N_{JF1F}$ or $N'_{J'F'} - N_{JF}$	[MHz]	[K]	[km.s^{-1}]	[km.s^{-1}]	[K.km.s^{-1}]
	$1_{1/2\ 0\ 1} - 0_{1/2\ 1\ 2}$	108426.89	5.23	11.4(0.3)	1.3(0.3)	0.07(0.01)
	$1_{3/2\ 1\ 0} - 0_{1/2\ 0\ 1}$	108631.12	5.21	11.7(0.4)	1.3(0.4)	0.04(0.02)
	$1_{3/2\ 1\ 1} - 0_{1/2\ 0\ 1}$	108636.92	5.21	11.3(0.3)	1.4(0.3)	0.11(0.02)
	$1_{3/2\ 1\ 2} - 0_{1/2\ 0\ 1}$	108651.30	5.21	11.5(0.3)	1.4(0.3)	0.18(0.03)
	$1_{1/2\ 1\ 2} - 0_{1/2\ 1\ 2}$	108657.65	5.24	11.4(0.3)	1.3(0.3)	0.13(0.02)
	$1_{3/2\ 2\ 3} - 0_{1/2\ 1\ 2}$	108780.20	5.25	11.4(0.3)	1.5(0.3)	0.27(0.05)
	$1_{3/2\ 2\ 2} - 0_{1/2\ 1\ 1}$	108782.37	5.25	11.4(0.3)	1.5(0.3)	0.16(0.03)
	$1_{3/2\ 2\ 1} - 0_{1/2\ 1\ 0}$	108786.98	5.25	11.3(0.3)	1.5(0.3)	0.06(0.01)
	$1_{3/2\ 2\ 1} - 0_{1/2\ 1\ 1}$	108793.75	5.25	11.3(0.3)	1.4(0.3)	0.06(0.01)
	$1_{3/2\ 2\ 2} - 0_{1/2\ 1\ 2}$	108796.40	5.25	11.4(0.4)	1.1(0.4)	0.05(0.02)
	$2_{5/2\ 3\ 3} - 1_{3/2\ 2\ 2}$	217467.15	15.69	11.3(0.1)	1.3(0.1)	0.36(0.08)
	$2_{5/2\ 3\ 2} - 1_{3/2\ 2\ 1}$	217469.15	15.69	11.2(0.1)	1.8(0.1)	0.23(0.05)
$C^{15}N$	$1_{1/2\ 1} - 0_{1/2\ 1}$	109689.61	5.27	11.1(0.4)	2.1(0.4)	0.05(0.02)
	$1_{3/2\ 1} - 0_{1/2\ 0}$	110023.54	5.28	11.5(0.3)	1.3(0.3)	0.05(0.02)
	$1_{3/2\ 2} - 0_{1/2\ 1}$	110024.59	5.28	11.4(0.4)	1.3(0.4)	0.08(0.02)
	$2_{3/2\ 2} - 1_{1/2\ 1}$	219722.49	15.81	11.3(0.2)	1.3(0.2)	0.08(0.02)
	$2_{5/2\ 2} - 1_{3/2\ 1}$	219934.04	15.84	11.4(0.1)	1.7(0.1)	0.10(0.03)

(1) For CN and ^{13}CN, according to the CDMS convention, the quantum numbers are N, J, F_1, F with $F_1 = J + I_1$, $F = F_1 + I_2$ where I_1 is the ^{12}C or ^{13}C nuclear spin and I_2 that of ^{14}N. For $C^{15}N$, the quantum numbers are N, J, F with J = N + S and F = J + I, where S and I are respectively the electronic spin and the nuclear spin of ^{15}N.

(2) The kinematical parameters and the integrated intensities correspond to the narrow Gaussian components only and the 1 σ error bars include the fit and the calibration uncertainties.

4. DISCUSSION AND CONCLUSIONS

4.1. *The $^{14}N/^{15}N$ ratio towards OMC-2 FIR4*

We have reported here a complete census of the $^{14}N/^{15}N$ ratio in the most abundant N-bearing species towards the protocluster OMC-2 FIR4. The five $^{14}N/^{15}N$ ratios derived directly from the line fluxes (HC_3N, CN, N_2H^+, $H^{13}CN$) appear very similar. Their weighted average is 260 ± 30. Two indirect $^{14}N/^{15}N$ ratio derivations, obtained with HCN and HNC, can be made from the double isotopic ratios $^{13}C^{14}N$ / $^{12}C^{15}N$. Discussing the $^{12}C/^{13}C$ isotopic ratio is outside of the scope of this study. However, it can just be noticed that one of the ^{13}C-bearing isotopologues of HC_3N seems to show systematically stronger lines than the two others (see Fig. 2) but this requires complementary observations to be confirmed and discussed. Although far from complete in terms of $^{12}C/^{13}C$ measurements, our data allow to derive five direct estimates of this isotopic ratio and its weighted average value is 50 ± 5. The resulting indirect $^{14}N/^{15}N$ ratios are respectively 270 ± 50 and 290 ± 50 for HCN and HNC. These values are in remarkable agreement with the direct determinations. The total weighted average including both direct and indirect measures is 270 ± 30. All the $^{14}N/^{15}N$ ratios derived in OMC-2 FIR4 are plotted in Fig. 3.

As discussed for each species, the narrow emission of HCN, HNC and CN, from which the $^{14}N/^{15}N$ ratio is measured, shows a very low excitation temperature (6 − 9 K). Without large scale emission maps for these species, we cannot firmly establish that they trace extended parent gas of the protocluster but it seems a reasonable interpretation. HC_3N narrow emission traces at least 2 components: a relatively cold gas (T_{ex} = 25K), that our recent observations obtained with the 30m telescope show to be extended, and a warmer component ($T_{ex} \sim 50$ K). A more sophisticated analysis of the HC_3N emission, included also the broad emission will be presented in a forthcoming article (Jaber Al-Edhari et al., in prep.). In addition, we also tentatively measured with the HCN isotopologues the $^{14}N/^{15}N$ ratio in the broad

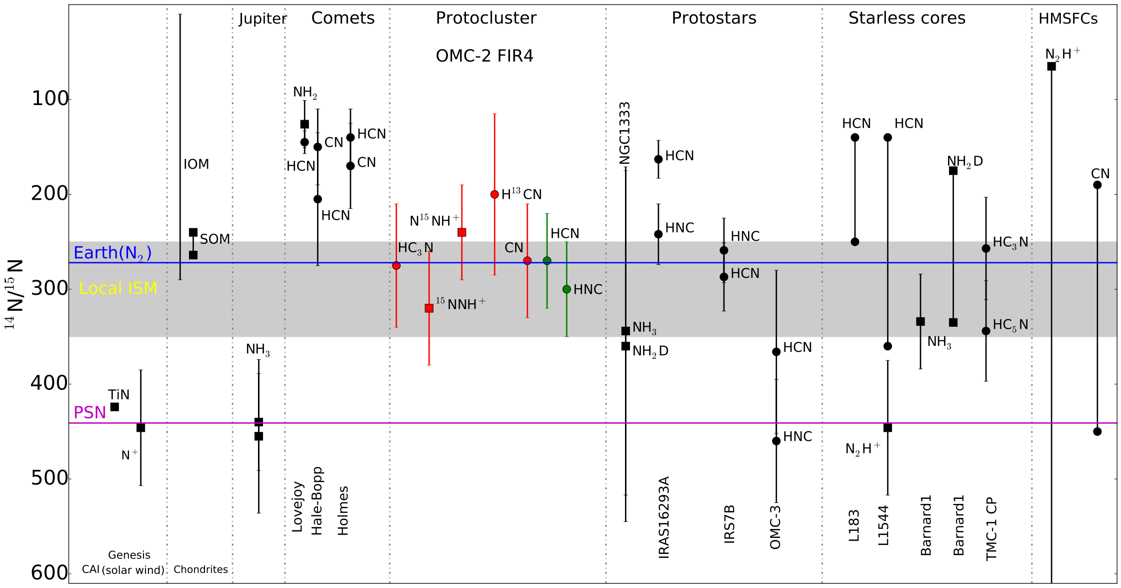

Figure 3. Nitrogen isotopic composition of Solar System objects compared with different sources (figure adapted from Hily-Blant et al. (2013)). The blue horizontal line represents the nitrogen isotopic composition of the terrestrial atmosphere($^{14}N/^{15}N$=272), while the magenta horizontal line indicates the protosolar nebula (PSN) value of 441 ± 6 Marty (2012). Square and circle symbols correspond to amine and nitrile functional groups, respectively. IOM means Insoluble Organic Matter, SOM Soluble Organic Matter, and CAI Calcium-, Aluminum-rich Inclusions. Red and green symbols represent respectively direct and indirect measurements of $^{14}N/^{15}N$ in OMC-2 FIR4, assuming $^{12}C/^{13}C = 50 \pm 5$ (this work). Protostars data are from Wampfler et al. (2014), starless cores data from Hily-Blant et al. (2013) and Taniguchi & Saito (2017), and high mass star forming cores data from Fontani et al. (2015) (where HMSC: high-mass starless core). The local galactic ratio range, shown as a grey zone, takes into account the measurements reported in Adande & Ziurys (2012) and Hily-Blant et al. (2017)

emission, detected for the main isotopologue of all the species studied here, except N_2H^+. This ratio appears perfectly compatible with the value derived from the narrow emission. Our data suggest that this broad emission is warmer than the narrow one but do not allow to estimate the emission size. We hope that the interferometric (ALMA and NOEMA) data that we will soon obtain towards this source will allow to understand the nature of this emission.

4.2. *Comparison with other galactic sources*

Measurements of the the $^{14}N/^{15}N$ ratio in starless cores (e.g. Hily-Blant et al. (2013)) and in protostars (e.g. Wampfler et al. (2014)) seem to indicate (see Fig. 3) that the ratios derived from molecules carrying the amine functional group (NH_3, N_2H^+) are larger than the ratios derived from molecules carrying the nitrile functional group (CN, HCN), a chemical origin being proposed for this effect. However, none of the studied sources shows a complete set of measurements from different tracers so that it is very difficult to distinguish between variations from source to source and from molecule to molecule. On the other hand, our results, which rely on a set of five different species that trace the same (cold extended) gas, and that belong to the nitrile and amine families, do not show any significant difference. In contrast, they are very similar, and they remarkably agree with the present local $^{14}N/^{15}N$ galactic ratio of ∼ 300 as derived from observations (Adande & Ziurys (2012); Hily-Blant et al. (2017) and references therein) and predicted by models of galactic CNO evolution (e.g. Romano et al. (2017)).

Our observations show that in OMC-2 FIR4, which is the best analogue of the Sun progenitor, there is no ^{15}N fractionation, compared to the nowadays value at the same (8 kpc) galactic center distance. This is in agreement with the recent model predictions by Roueff et al. (2015).

In conclusion, the presented measurements of $^{14}N/^{15}N$ seem to be at odd with the previous measurements in prestellar cores and protostars (see Fig. 3), which, depending on the used species, suggest ^{15}N enrichment or deficiency with respect to the local ISM value. It is possible that this discrepancy is due to the different spatial scale probed by our and the others observations. Specifically, while the cold and large scale gas might not be ^{15}N enriched, local smaller scale clumps might present this enrichment (or deficiency). On going interferometric observations towards

OMC-2 FIR4 will verify this possibility. If this is the case, the enrichment of the Solar System bodies could find an explanation in the ISM chemistry. If, on the contrary, the new observations would confirm the absence of ^{15}N enrichment also at small scales, then the ^{15}N enrichment in Solar System bodies must have another nature.

ACKNOWLEDGEMENTS

We acknowledge the financial support from the university of Al-Muthanna and the ministry of higher education and scientific research in Iraq. We acknowledge the funding from the European Research Council (ERC), project DOC (the Dawn of Organic Chemistry), contract number 741002. We warmly thank Pierre Hily-Blant for fruitful discussions.

Software: CASSIS (Vastel et al. 2015), GILDAS

APPENDIX

A. OBSERVED LINES

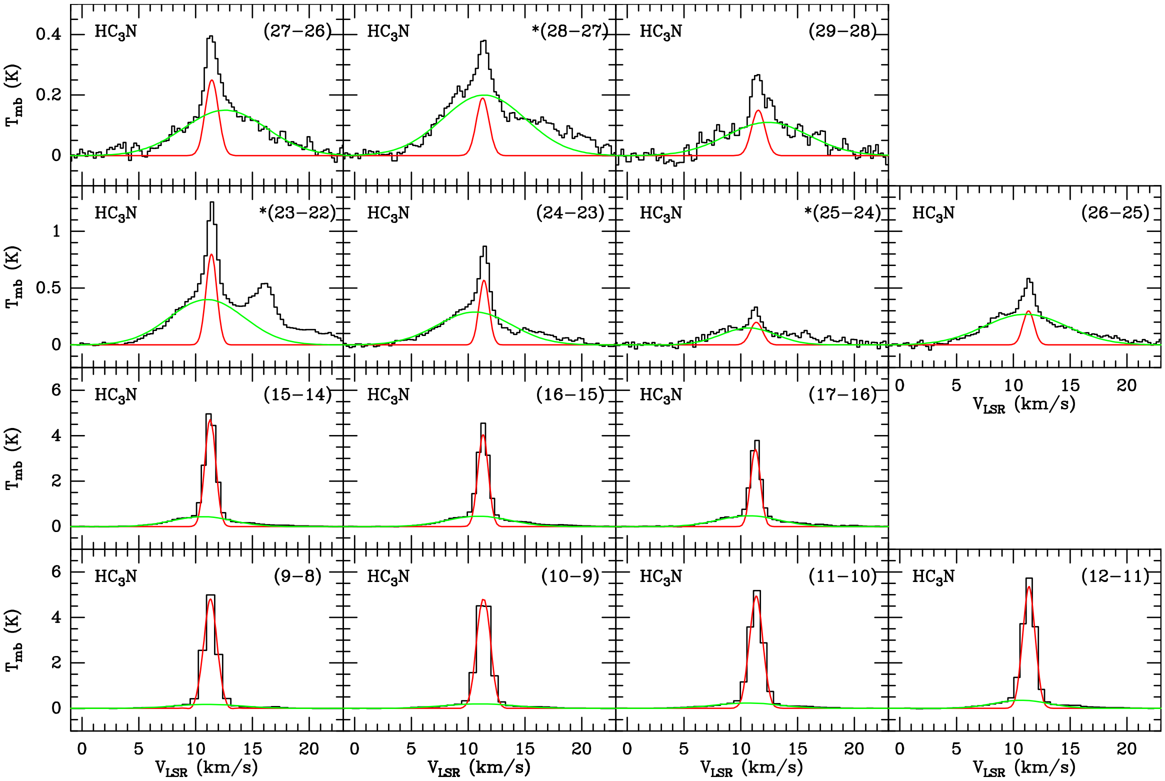

Figure 4. HC$_3$N observed spectra and two components Gaussian fits to the lines. The temperature scale is main beam temperature. Due to significant overlaping with other emissions or calibration problem, the lines indicated by an asterisc (*) have not been included in our analysis nor reported in Table 1.

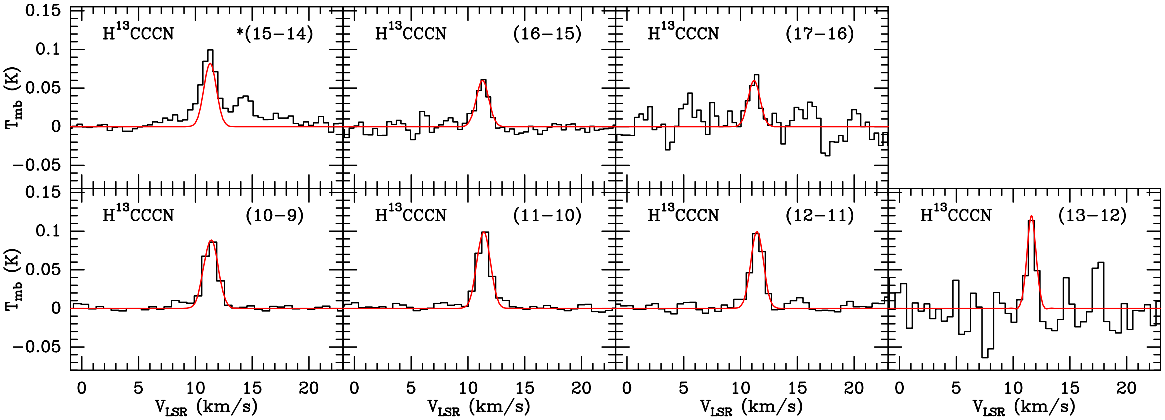

Figure 5. H^{13}CCCN observed spectra and Gaussian fit to the lines. The temperature scale is main beam temperature. Due to significant overlaping with other emissions the line indicated by an asterisc (*) has not been included in our analysis nor reported in Table 1.

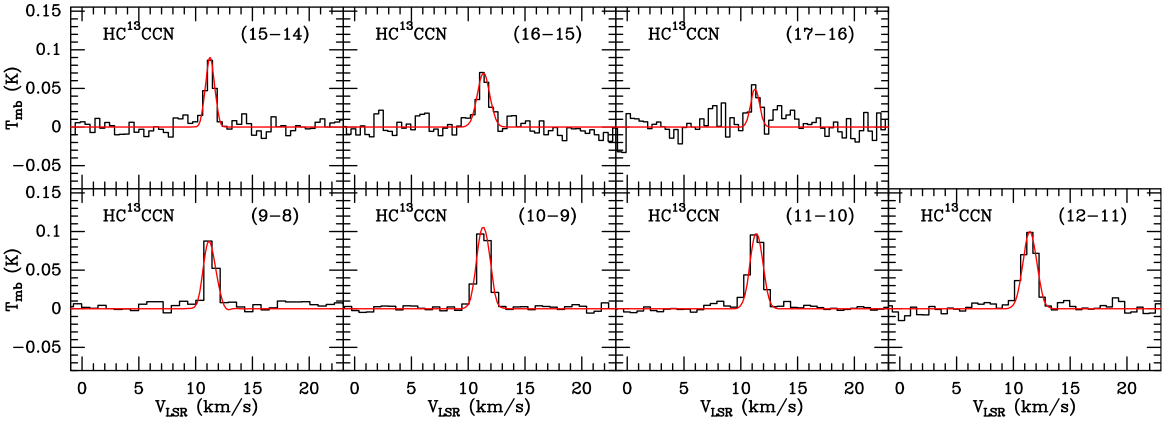

Figure 6. HC^{13}CCN observed spectra and Gaussian fit to the lines. The temperature scale is main beam temperature.

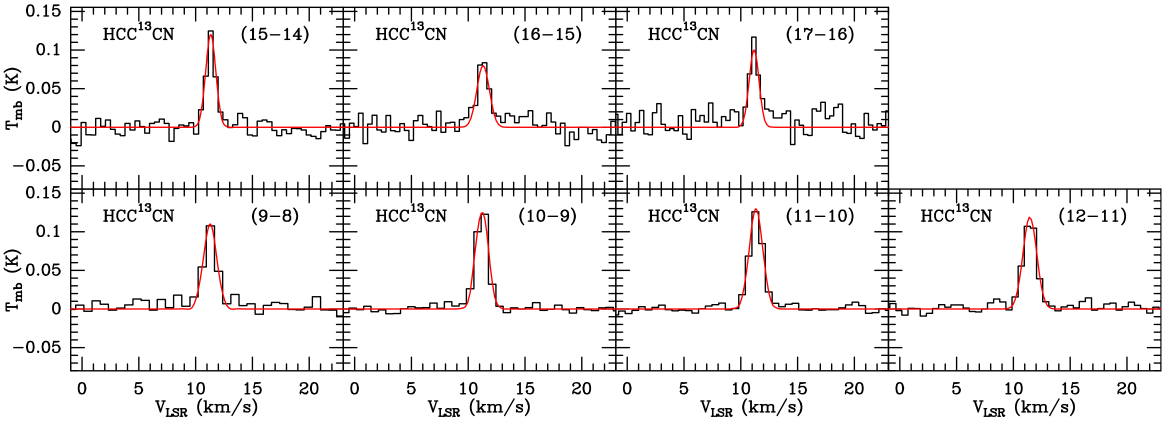

Figure 7. HCC^{13}CN observed spectra and Gaussian fit to the lines. The temperature scale is main beam temperature.

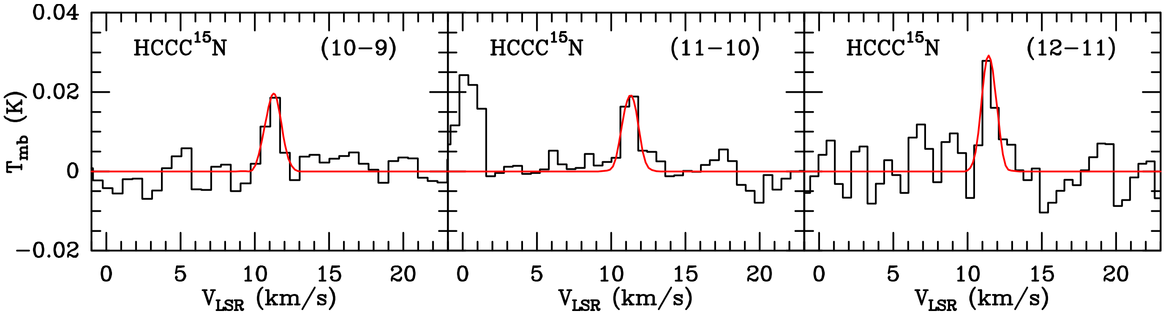

Figure 8. HCCC^{15}N observed spectra and Gaussian fit to the lines. The temperature scale is main beam temperature.

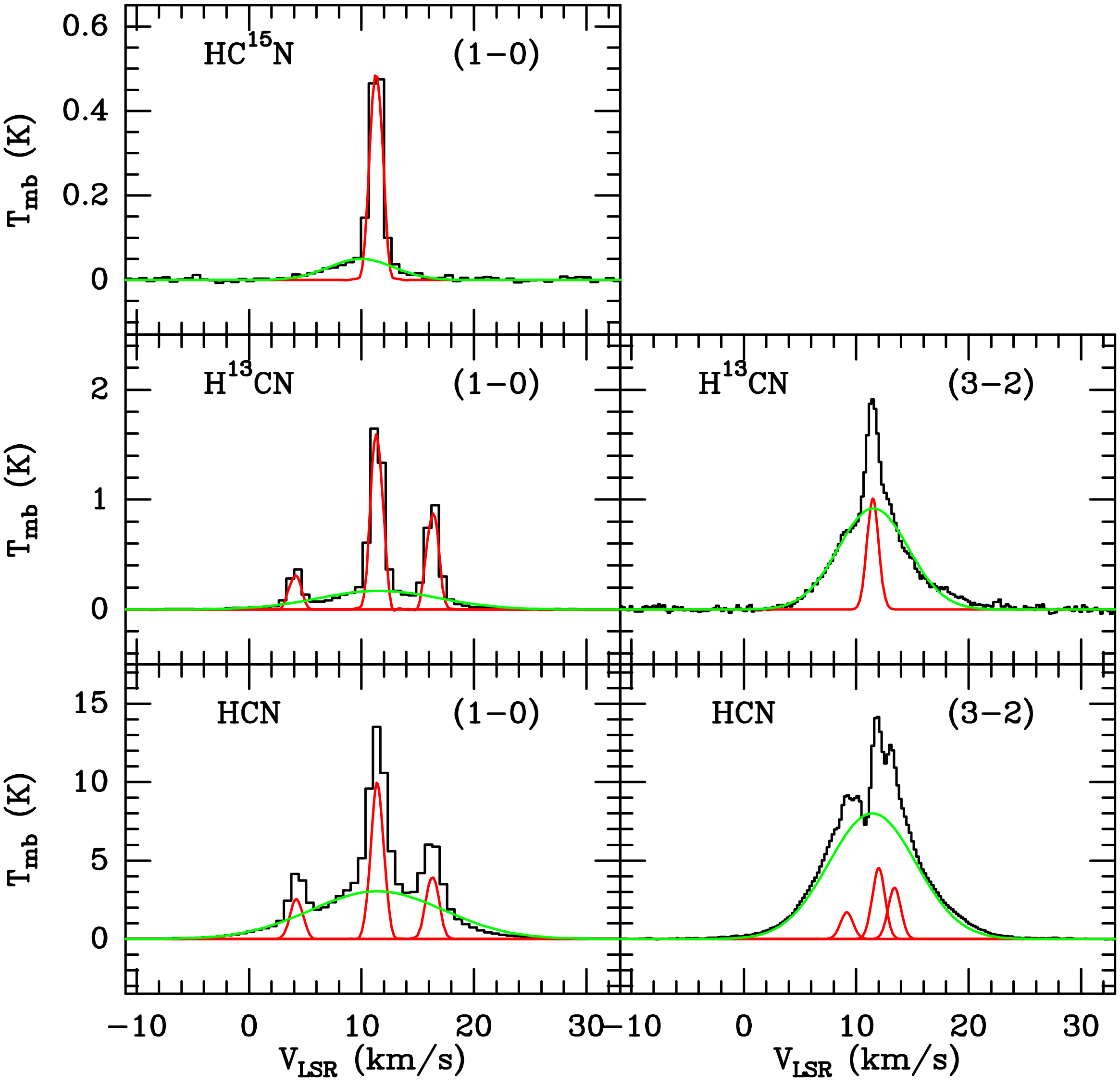

Figure 9. HCN and its isotopologues observed spectra. Two components Gaussian fits to the lines are superimposed to the spectra. The temperature scale is main beam temperature.

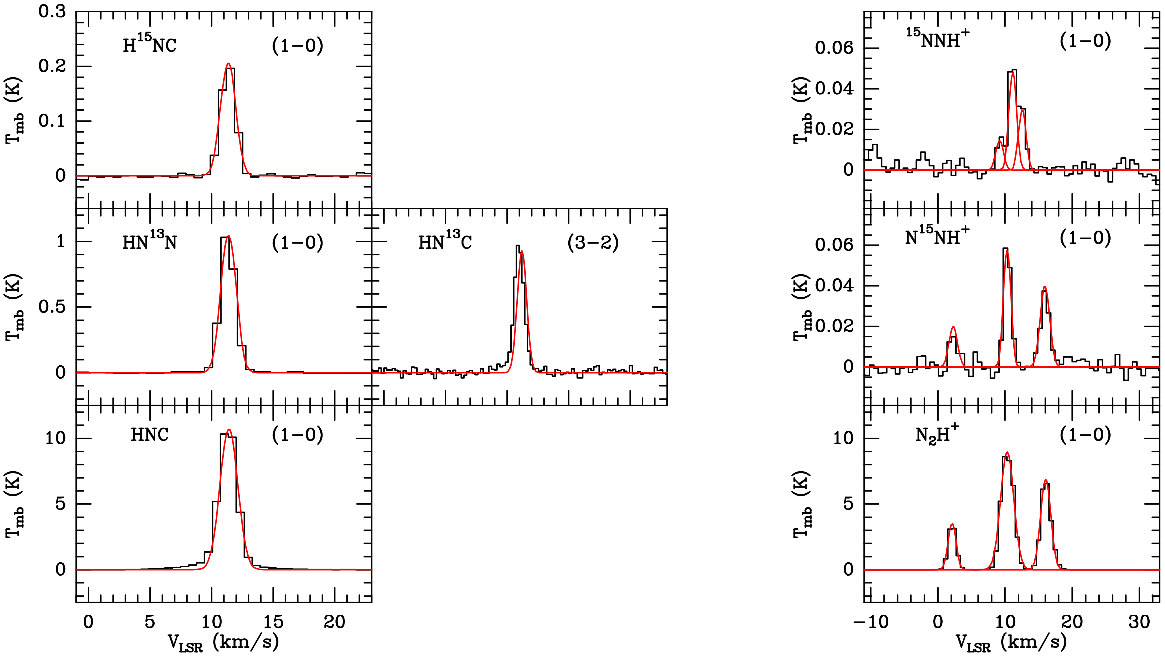

Figure 10. HNC, N_2H^+ and their isotopologues observed spectra. Gaussian fits to the lines are superimposed to the spectra. The temperature scale is main beam temperature.

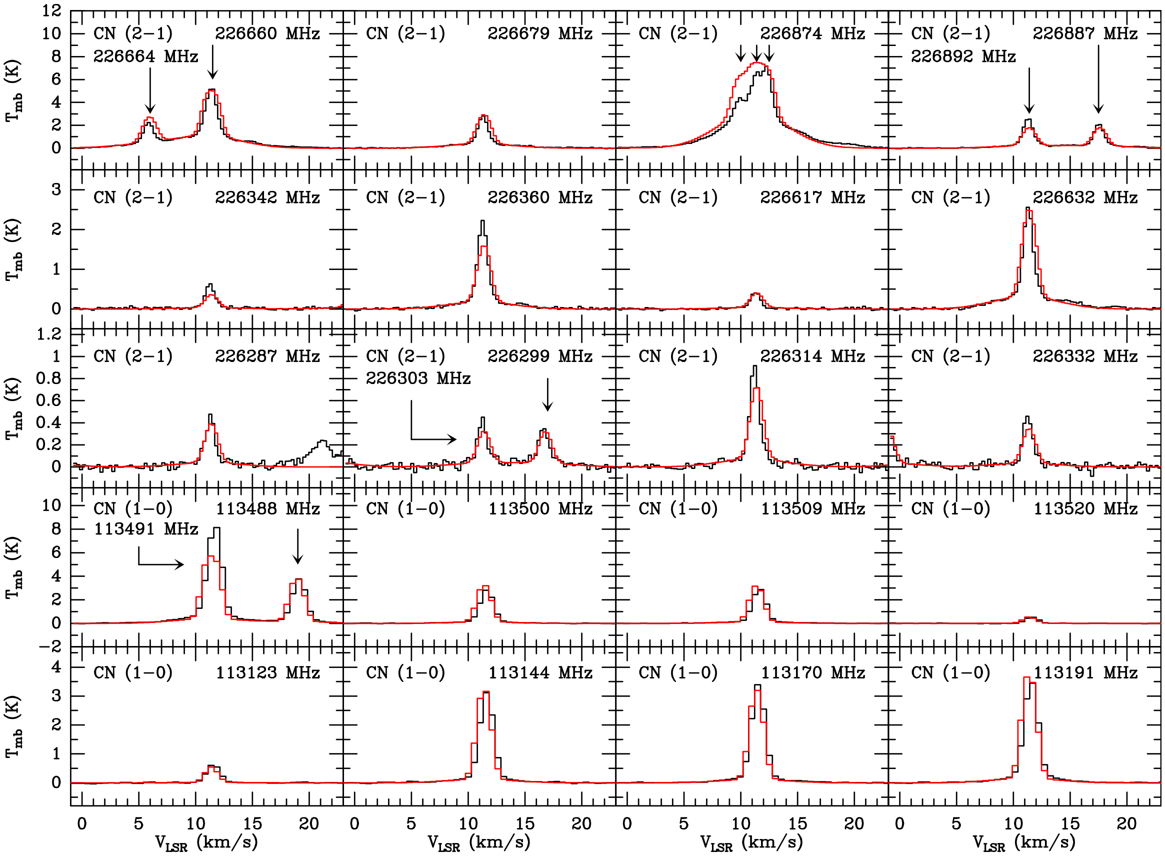

Figure 11. CN observed spectra. The profiles superimposed to the spectra have been calculated with a two components LTE modeling (see text). When several close hyperfine components are present, the frequency of the main one is given. The temperature scale is main beam temperature.

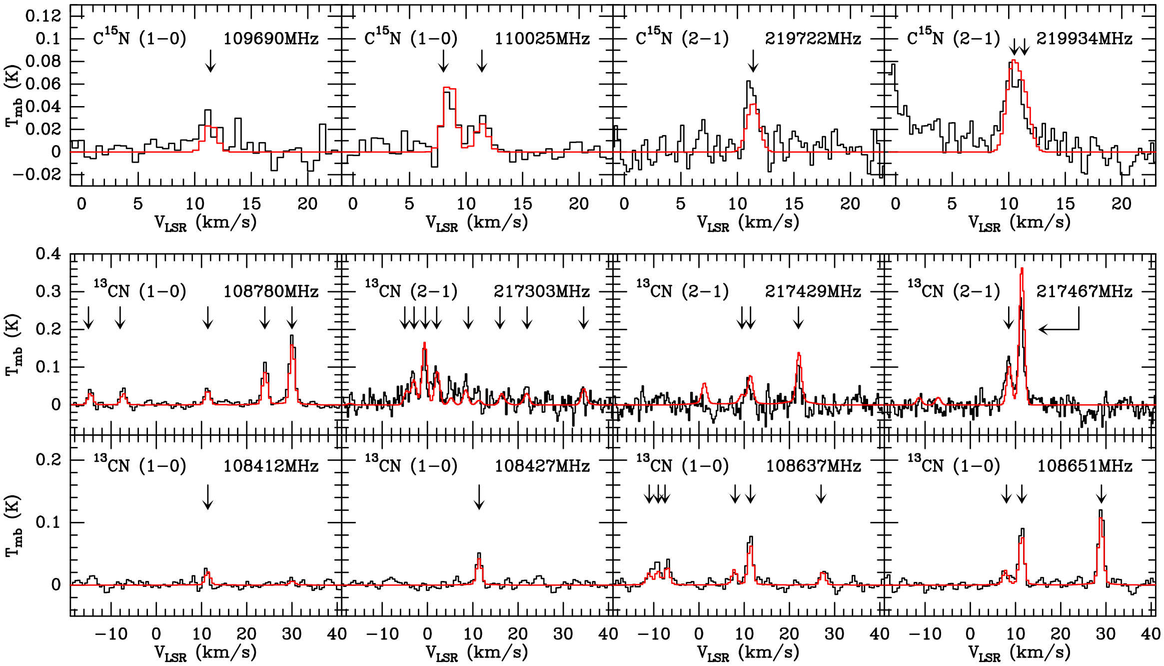

Figure 12. ^{13}CN and C^{15}Nobserved spectra. The profiles superimposed to the spectra have been calculated with a LTE modeling (see text). When several close hyperfine components are present, the frequency of the main one is given. The temperature scale is main beam temperature.

B. OPACITY CHECKS OF HYPERFINE COMPONENTS

Table 5. Relative fluxes of the hyperfine components.

Species	Transition	Frequency [MHz]	E$_{up}$ [K]	g$_{up}$	A$_{ij}$ [s^{-1}]	R_theo.$^{(1)}$	$\int$T$_{mb}$dv$^{(2)}$ [K.km.s^{-1}]	R_obs.$^{(3)}$
HCN	$1_1 - 0_1$	88630.42	4.25	3	2.43×10^{-5}	3.0	8.4(0.9)	1.6(0.2)
	$1_2 - 0_1$	88631.85	4.25	5	2.43×10^{-5}	5.0	13.5(2.0)	2.6(0.5)
	$1_0 - 0_1$*	88633.94	4.25	1	2.43×10^{-5}	1.0	5.2(0.5)	1.0(0.1)
H^{13}CN	$1_1 - 0_1$	86338.77	4.14	3	2.22×10^{-5}	3.0	1.3(0.1)	2.9(0.5)
	$1_2 - 0_1$	86340.18	4.14	5	2.22×10^{-5}	5.0	2.2(0.2)	5.1(0.9)
	$1_0 - 0_1$*	86342.27	4.14	1	2.22×10^{-5}	1.0	0.44(0.06)	1.0(0.2)
NNH$^+$	$1_1 - 0_1$	93171.88	4.47	9	3.63×10^{-5}	3.0	13.1(1.5)	2.5(0.4)
	$1_2 - 0_1$	93173.70	4.47	15	3.63×10^{-5}	5.0	21.3(2.5)	4.1(0.6)
	$1_0 - 0_1$*	93176.13	4.47	3	3.63×10^{-5}	1.0	5.3(0.5)	1.0(0.1)
^{15}NNH$^+$	$1_2 - 0_1$	90263.91	4.38	3	3.30×10^{-5}	3.0	0.036(0.005)	2.4(0.7)
	$1_1 - 0_1$	90263.49	4.38	5	3.30×10^{-5}	5.0	0.08(0.01)	5.0(1.5)
	$1_0 - 0_1$*	90264.50	4.38	1	3.30×10^{-5}	1.0	0.015(0.004)	1.0(0.4)
N^{15}NH$^+$	$1_1 - 0_1$	91204.26	4.33	3	3.40×10^{-5}	3.0	0.059(0.008)	2.4(0.6)
	$1_2 - 0_1$	91205.99	4.33	5	3.40×10^{-5}	5.0	0.09(0.02)	3.8(1.2)
	$1_0 - 0_1$*	91208.52	4.33	1	3.40×10^{-5}	1.0	0.025(0.006)	1.0(0.3)
CN	$1_{0\ 1/2\ 1/2} - 0_{0\ 1/2\ 1/2}$*	113123.37	5.43	2	1.29×10^{-6}	1.0	0.9(0.1)	1.1(0.2)
	$1_{0\ 1/2\ 1/2} - 0_{0\ 1/2\ 3/2}$	113144.19	5.43	2	1.05×10^{-5}	8.1	4.9(0.5)	5.8(0.8)
	$1_{0\ 1/2\ 3/2} - 0_{0\ 1/2\ 1/2}$	113170.54	5.43	4	5.14×10^{-6}	7.9	5.3(0.5)	6.2(0.9)
	$1_{0\ 1/2\ 3/2} - 0_{0\ 1/2\ 3/2}$	113191.33	5.43	4	6.68×10^{-6}	10.3	5.6(0.6)	6.6(1.0)
	$1_{0\ 3/2\ 3/2} - 0_{0\ 1/2\ 1/2}$	113488.14	5.45	4	6.73×10^{-6}	10.4	6.0(0.7)	7.0(1.1)
	$1_{0\ 3/2\ 5/2} - 0_{0\ 1/2\ 3/2}$	113490.99	5.45	6	1.19×10^{-5}	27.5	14.0(1.6)	16.4(2.5)
	$1_{0\ 3/2\ 1/2} - 0_{0\ 1/2\ 1/2}$	113499.64	5.45	2	1.06×10^{-5}	8.2	4.3(0.4)	5.1(0.7)
	$1_{0\ 3/2\ 3/2} - 0_{0\ 1/2\ 3/2}$	113508.93	5.45	4	5.19×10^{-6}	8.0	4.5(0.5)	5.3(0.8)
	$1_{0\ 3/2\ 1/2} - 0_{0\ 1/2\ 3/2}$*	113520.42	5.45	2	1.30×10^{-6}	1.0	0.76(0.08)	0.9(0.1)
	$2_{0\ 3/2\ 1/2} - 1_{0\ 3/2\ 1/2}$	226287.43	16.31	2	1.03×10^{-5}	4.6	0.5(0.1)	5.1(1.1)
	$2_{0\ 3/2\ 1/2} - 1_{0\ 3/2\ 3/2}$	226298.92	16.31	2	8.23×10^{-6}	3.7	0.6(0.2)	5.8(1.7)
	$2_{0\ 3/2\ 3/2} - 1_{0\ 3/2\ 1/2}$	226303.08	16.31	4	4.17×10^{-6}	3.7	0.5(0.1)	4.9(1.2)
	$2_{0\ 3/2\ 3/2} - 1_{0\ 3/2\ 3/2}$	226314.54	16.31	4	9.91×10^{-6}	8.8	1.0(0.2)	10.1(2.1)
	$2_{0\ 3/2\ 3/2} - 1_{0\ 1/2\ 5/2}$	226332.54	16.31	4	4.55×10^{-6}	4.0	0.5(0.1)	5.0 (1.1)
	$2_{0\ 3/2\ 5/2} - 1_{0\ 3/2\ 3/2}$	226341.93	16.31	6	3.16×10^{-6}	4.2	0.7(0.1)	6.6(1.4)
	$2_{0\ 3/2\ 5/2} - 1_{0\ 3/2\ 5/2}$	226359.87	16.31	6	1.61×10^{-5}	21.4	2.6(0.6)	25.4(5.3)
	$2_{0\ 3/2\ 1/2} - 1_{0\ 1/2\ 3/2}$	226616.56	16.31	2	1.07×10^{-5}	4.8	0.5(0.1)	4.6(0.9)
	$2_{0\ 3/2\ 3/2} - 1_{0\ 1/2\ 3/2}$	226632.19	16.31	4	4.26×10^{-5}	37.9	3.2(0.7)	31.2(6.8)
	$2_{0\ 3/2\ 5/2} - 1_{0\ 1/2\ 3/2}$	226659.58	16.31	6	9.47×10^{-5}	126.2	8.3(1.7)	80(17)
	$2_{0\ 3/2\ 1/2} - 1_{0\ 1/2\ 1/2}$	226663.70	16.31	2	8.46×10^{-5}	37.6	3.2(0.7)	30.9(6.6)
	$2_{0\ 3/2\ 3/2} - 1_{0\ 1/2\ 1/2}$	226679.38	16.31	4	5.27×10^{-5}	46.8	3.6(0.8)	35.0 (7.3)

Continued on next page

series Table 5 – continued from previous page

Species	Transition	Frequency [MHz]	E$_{up}$ [K]	g$_{up}$	A$_{ij}$ [S^{-1}]	R_theo.$^{(1)}$	$\int$T$_{mb}$dv$^{(2)}$ [K.km.s^{-1}]	R_obs.$^{(3)}$
	$2_{0\ 5/2\ 5/2} - 1_{0\ 3/2\ 5/2}$	226892.12	16.34	6	1.81×10^{-5}	24.1	3.2(0.7)	30.9 (6.5)
	$2_{0\ 5/2\ 3/2} - 1_{0\ 3/2\ 5/2}{}^*$	226905.38	16.34	4	1.13×10^{-6}	1.0	0.10(0.03)	1.0(0.3)
^{13}CN	$1_{1/2\ 0\ 1} - 0_{1/2\ 1\ 1}$	108412.86	5.23	3	3.1×10^{-6}	1.1	0.03(0.01)	1.1(0.5)
	$1_{1/2\ 0\ 1} - 0_{1/2\ 1\ 2}$	108426.89	5.23	3	6.3×10^{-6}	2.3	0.069(0.008)	2.1(0.7)
	$1_{1/2\ 1\ 0} - 0_{1/2\ 0\ 1}$	108631.12	5.21	1	9.6×10^{-6}	1.2	0.04(0.02)	1.1(0.7)
	$1_{1/2\ 1\ 1} - 0_{1/2\ 0\ 1}$	108636.92	5.21	3	9.6×10^{-6}	3.5	0.11(0.02)	3.4(1.1)
	$1_{1/2\ 1\ 2} - 0_{1/2\ 0\ 1}$	108651.30	5.21	5	9.8×10^{-6}	5.9	0.18(0.03)	5.4(1.9)
	$1_{3/2\ 1\ 2} - 0_{1/2\ 1\ 2}$	108657.65	5.24	5	7.2×10^{-6}	4.4	0.13(0.02)	4.0(1.3)
	$1_{3/2\ 2\ 3} - 0_{1/2\ 1\ 2}$	108780.20	5.25	7	1.1×10^{-5}	8.9	0.27(0.05)	8.2(2.8)
	$1_{3/2\ 2\ 2} - 0_{1/2\ 1\ 1}$	108782.37	5.25	5	7.8×10^{-6}	4.7	0.16(0.03)	4.9(1.6)
	$1_{3/2\ 2\ 1} - 0_{1/2\ 1\ 0}$	108786.98	5.25	3	5.7×10^{-6}	2.1	0.06(0.01)	2.0(0.7)
	$1_{3/2\ 2\ 1} - 0_{1/2\ 1\ 1}$	108793.75	5.25	3	4.5×10^{-6}	1.6	0.06(0.01)	1.9(0.6)
	$1_{3/2\ 2\ 2} - 0_{1/2\ 1\ 2}$	108796.40	5.25	5	2.8×10^{-6}	1.7	0.05(0.02)	1.7(0.8)
	$1_{3/2\ 1\ 2} - 0_{1/2\ 1\ 1}$	108643.59	5.24	5	2.6×10^{-6}	1.6	0.06(0.01)	1.7(0.6)
	$1_{3/2\ 1\ 0} - 0_{1/2\ 1\ 1}$	108644.35	5.24	1	9.6×10^{-6}	1.2	0.06(0.02)	1.8(0.7)
	$1_{3/2\ 1\ 1} - 0_{1/2\ 1\ 1}{}^*$	108645.06	5.24	3	2.7×10^{-6}	1.0	0.03(0.01)	1.0(0.4)
	$1_{3/2\ 1\ 1} - 0_{1/2\ 1\ 2}$	108658.95	5.24	3	3.3×10^{-6}	1.2	0.03(0.01)	1.0(0.5)
	$2_{5/2\ 3\ 3} - 1_{3/2\ 2\ 2}$	217467.15	15.69	7	8.92×10^{-5}	0.6	0.36(0.08)	0.6(0.1)
	$2_{5/2\ 3\ 2} - 1_{3/2\ 2\ 1}$	217469.15	15.69	5	8.43×10^{-5}	0.4	0.23(0.05)	0.4(0.1)
C^{15}N	$1_{1/2\ 1} - 0_{1/2\ 1}{}^*$	109689.61	5.27	3	7.10×10^{-6}	1.0	0.05(0.02)	1.0(0.5)
	$1_{3/2\ 1} - 0_{1/2\ 1}$	110023.54	5.28	3	7.16×10^{-6}	1.0	0.05(0.02)	1.0(0.4)
	$1_{3/2\ 2} - 0_{1/2\ 1}$	110024.59	5.28	5	1.09×10^{-5}	2.6	0.08(0.02)	1.7(0.7)
	$2_{3/2\ 2} - 1_{1/2\ 1}$	219722.49	15.81	5	8.67×10^{-5}	0.3	0.08(0.02)	0.4(0.1)
	$2_{5/2\ 2} - 1_{3/2\ 1}$	219934.04	15.84	5	9.36×10^{-5}	0.7	0.10(0.03)	0.6(0.1)

[*] Weakest detected line of the hyperfine structure. This is the reference to compute R$_{theo}$ and R$_{obs}$

[1] Ratio of the line G$_{up}$ A$_{ij}$ product relative to the reference line; equal to the fluxes ratio in LTE optically thin conditions, neglecting the frequency differences.

[2] Observed lines fluxes derived from gaussian fits ; the errors include fit and calibration uncertainties.

[3] Ratio of observed fluxes relative to the reference line. For CN ($N = 1 - 0$), the reference flux is averaged over the 2 reference lines.

REFERENCES

Adande, G. R., & Ziurys, L. M. 2012, ApJ, 744, 194

Aléon, J. 2010, ApJ, 722, 1342

Bizzocchi, L., Caselli, P., Leonardo, E., & Dore, L. 2013, A&A, 555, A109

Bonal, L., Huss, G. R., Krot, A. N., et al. 2010, GeoCoA, 74, 6590

Busemann, H., Alexander, C. M. O., Nittler, L. R., et al. 2006, Meteoritics and Planetary Science Supplement, 41, 5327

Caselli, P., & Ceccarelli, C. 2012, A&A Rv, 20, 56

Ceccarelli, C., Caselli, P., Bockelée-Morvan, D., et al. 2014a, Protostars and Planets VI, 859

Ceccarelli, C., Dominik, C., López-Sepulcre, A., et al. 2014b, ApJ, 790, L1

Cleeves, L. I., Bergin, E. A., Qi, C., Adams, F. C., & Öberg, K. I. 2015, ApJ, 799, 204

Daniel, F., Gérin, M., Roueff, E., et al. 2013, A&A, 560, A3

Dore, L., Bizzocchi, L., Degli Esposti, C., & Tinti, F. 2009, A&A, 496, 275

Fontani, F., Caselli, P., Palau, A., Bizzocchi, L., & Ceccarelli, C. 2015, ApJL, 808, L46

Fontani, F. Ceccarelli, C., Favre, C., Caselli, P., Neri, R., Sims, I. R., Kahane, C., Alves, F. O., Balucani, N., Bianchi, E., et al. 2017, A&A, 605, 57

Furlan, E., Megeath, S. T., Osorio, M., et al. 2014, ApJ, 786, 26

Gerin, M., Marcelino, N., Biver, N., et al. 2009, A&A, 498, L9

Guzmán, V. V., Öberg, K. I., Loomis, R., & Qi, C. 2015, ApJ, 814, 53

Guzmán, V. V., Öberg, K. I., Huang, J., Loomis, R., & Qi, C. 2017, ApJ, 836, 30

Hily-Blant, P., Bonal, L. Faure, A. & Quirico, E. 2013, Icarus, 223, 582

Hily-Blant, P., Magalhaes, V., Kastner, J., Faure, A. Forveille, T., & Qi, C. 2017, A&A, 603, L6.

Hirota, T., Bushimata, T., Choi, Y. K., et al. 2007, PASJ, 59, 897

Ikeda, M., Hirota, T., & Yamamoto, S. 2002, ApJ, 575, 250

López-Sepulcre, A., Taquet, V., Sánchez-Monge, Á., et al. 2013, A&A, 556, A62

Manfroid, J., Jehin, E., Hutsemékers, D., et al. 2009, A&A, 503, 613

Marty, B. 2012, Earth Planet Sci Lett 313, 56

Menten, K. M., Reid, M. J., Forbrich, J., & Brunthaler, A. 2007, A&A, 474, 515

Milam, S. N., & Charnley, S. B. 2012, in Lunar and Planetary Science Conference, Vol. 43, Lunar and Planetary Science Conference, 2618

Mumma, M. J., & Charnley, S. B. 2011, ARA&A, 49, 471

Rodgers, S. D., & Charnley, S. B. 2008, ApJ, 689, 1448

Romano, D., Matteucci, F., Zhang, Z.-Y., Papadopoulos, P. P., & Ivison, R. J. 2017, MNRAS, 470, 401

Roueff, E., Loison, J. C., & Hickson, K. M. 2015, A&A, 576, A99

Rousselot, P., Pirali, O., Jehin, E., et al. 2014, ApJL, 780, L17

Shimajiri, Y., Takahashi, S., Takakuwa, S., Saito, M., & Kawabe, R. 2008, ApJ, 683, 255

Shinnaka, Y., Kawakita, H., Kobayashi, H., Nagashima, M., & Boice, D. C. 2014, ApJL, 782, L16

Taniguchi, K., & Saito, M. 2017, ArXiv e-prints, arXiv:1706.08662

Terzieva, R., & Herbst, E. 2000, MNRAS, 317, 563

Vastel, C., Bottinelli, S., Caux, E., Glorian, J.-M., & Boiziot, M. 2015, Proceedings of the Annual meeting of the French Society of Astronomy and Astrophysics. Eds.: F. Martins, S. Boissier, V. Buat, L. Cambrsy, P. Petit, pp.313-316

Wampfler, S. F., Jørgensen, J. K., Bizzarro, M., & Bisschop, S. E. 2014, A&A, 572, A24

Wirström, E. S., Charnley, S. B., Cordiner, M. A., & Milam, S. N. 2012, ApJL, 757, L11